

General solution for the complex frequency shift in microwave measurements of thin films

Peligrad, D.-N.; Nebendahl, B.; Mehring, M.; Dulčić, Antonije; Požek, Miroslav; Paar, Dalibor

Source / Izvornik: **Physical review B: Condensed matter and materials physics**, 2001, **64**, 224504 - 12

Journal article, Published version

Rad u časopisu, Objavljena verzija rada (izdavačev PDF)

<https://doi.org/10.1103/PhysRevB.64.224504>

Permanent link / Trajna poveznica: <https://urn.nsk.hr/urn:nbn:hr:217:219108>

Rights / Prava: [In copyright](#) / [Zaštićeno autorskim pravom.](#)

Download date / Datum preuzimanja: **2025-03-23**



Repository / Repozitorij:

[Repository of the Faculty of Science - University of Zagreb](#)



General solution for the complex frequency shift in microwave measurements of thin films

D.-N. Peligrad,^{*,†} B. Nebendahl,[‡] and M. Mehring
2. Physikalisches Institut, Universität Stuttgart, D-70550 Stuttgart, Germany

A. Dulčić,[†] M. Požek, and D. Paar
Department of Physics, Faculty of Science, University of Zagreb, POB 331, 10002 Zagreb, Croatia
 (Received 30 May 2001; published 20 November 2001)

Perturbation of a microwave cavity by a small sample with variable dielectric, magnetic, or conducting properties is considered. The complex frequency shift is derived in terms of a volume integral, or equivalently, in terms of a surface integral. These are used to obtain a general formula for thin films in the microwave electric field maximum. The complex frequency shift depends on the depolarization factor of the film and on its thickness in a nontrivial way. The previously known expressions for the complex frequency shift are shown to be good approximations of the present solution in the low and high conductivity limits. Our formula is applied to calculate the signal shapes in superconducting films of various geometric parameters and conductivities. It is shown that a diversity of signal shapes can result, and experimental support of those shapes is provided. The role of the dielectric substrate on which the thin film is grown is simply reduced to an asymmetry effect.

DOI: 10.1103/PhysRevB.64.224504

PACS number(s): 74.25.Nf, 74.76.Bz

I. INTRODUCTION

Microwave measurements have shown to be very useful in probing the superconducting state in high-temperature superconductors.^{1–12} The measured quantities are the shifts of the resonance frequency and the Q factor of the microwave cavity loaded with a sample. In order to extract the real and imaginary parts of the complex conductivity $\tilde{\sigma} = \sigma_1 - i\sigma_2$ from the measured shifts, one needs an accurate expression for the cavity perturbation by the sample. This is an old problem which has been extensively treated in the literature.^{13–19} The general perturbation formula involves both, perturbed and unperturbed fields, and can be considered as satisfactory if the perturbed fields are not much changed with respect to the unperturbed. When the sample is a weak dielectric, it is justified to take the empty cavity as the unperturbed state, so that the insertion of the sample makes a small perturbation. However, the insertion of a good conductor sample into the cavity changes the fields considerably and cannot be treated as a small perturbation. It was proposed to treat the cavity loaded with a perfect conductor sample as the unperturbed state, and find the shifts when the sample becomes a nonperfect conductor.²⁰ Thus, one may expect that the small perturbation condition will hold again.

When the integrals in the perturbation expression have to be calculated specifically, one needs to know the sample shape. The problem was analytically tractable only for a spherical sample.^{21,22} Shchegolev has found a practical solution for the complex frequency shift with ellipsoidal samples in the microwave electric field which fully penetrates the sample.^{23,24} This is the depolarization regime which has proven to be applicable in many studies.^{25,26} Obviously, one may expect that the Shchegolev formula becomes gradually incorrect as the conductivity of the sample is increased so that one passes through the depolarization crossover and beyond it. The discrepancy was demonstrated on a spherical conducting sample in the microwave electric field.^{20,27}

In the limit of very high conductivities and/or thick

samples, the microwave penetration depth becomes smaller than the size of the sample. This is known as the skin depth regime where the complex frequency shift can be related to the surface impedance of the sample.^{17–20} Usually, single crystals of high- T_c superconductors are thick enough so that the skin depth limit is valid at frequencies of 10 GHz or higher, and the analysis using the surface impedance formula can be applied.^{5–10}

In a previous paper,²⁸ we treated the problem of thin films which had high enough conductivities to be well above the depolarization crossover. The theoretical solutions predicted a sharp negative peak in the frequency shift just below the superconducting transition temperature T_c in agreement with the experimental observations.²⁸ Those solutions also included the correct behavior in the skin depth limit.

Generally, thin films can have different thicknesses and conductivities so that the samples may appear anywhere between the depolarization regime and the regime which is close to the skin depth limit. In such cases, using either the Shchegolev formula^{23–26} or the formula derived in our previous paper²⁸ would yield incorrect values for the complex conductivity $\tilde{\sigma} = \sigma_1 - i\sigma_2$ of the material. Consequently, the physical conclusions drawn from the complex conductivity would be erroneous.

In the present paper we review the cavity perturbation problem and the depolarization in ac fields. We find a general solution for the complex frequency shift which reduces to the Shchegolev formula²³ in the depolarization limit and to the formula given in our previous paper²⁸ in the high-conductivity limit.

II. CAVITY PERTURBATION

The influence of a small variation of the parameters on the properties of a resonant cavity was first studied by Müller.²⁹ Solutions were derived for the resonant frequency shift in cases when the walls of the cavity are perturbed, or a sample is introduced in the cavity.^{16–19} Here, we are interested in the

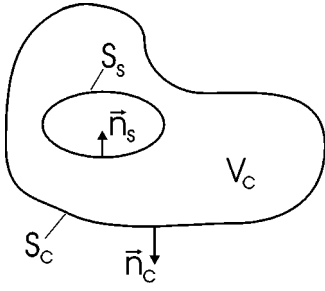


FIG. 1. Microwave cavity with a sample inside it. S_c is the surface of the cavity walls, \mathbf{n}_c is the unit vector normal to this surface, and V_c is the cavity volume. The surface of the sample is denoted by S_s , and the unit vector normal to it by \mathbf{n}_s .

complex frequency shift, which includes both, losses and resonant frequency shift, when the properties of the sample are changed. One may consider the complex quantity

$$\tilde{\Phi} = - \oint_{S_c} (\mathbf{E} \times \mathbf{H}^*) \cdot \mathbf{n}_c dS = - \int_{V_c} \nabla \cdot (\mathbf{E} \times \mathbf{H}^*) dV, \quad (1)$$

where S_c is the surface of the cavity walls, \mathbf{n}_c is the unit vector normal to this surface, and V_c is the cavity volume (Fig. 1). Losses could occur in the cavity walls, or in the sample placed inside the cavity, or in both. This is accounted for by writing the time dependence of the fields as $\exp(i\tilde{\omega}t)$, where $\tilde{\omega} = \omega(1 + i/2Q)$ is the complex frequency, and Q is the resulting Q factor of the cavity loaded with the sample. Using the Maxwell equations one obtains

$$\tilde{\Phi} = i \int_{V_c} (\tilde{\omega} \mathbf{H}^* \cdot \mathbf{B} - \tilde{\omega}^* \mathbf{E} \cdot \mathbf{D}^*) dV. \quad (2)$$

If the properties of the sample are changed, each of the fields is changed as $\mathbf{F} \rightarrow \mathbf{F} + \delta\mathbf{F}$. The new complex frequency can be written as $\tilde{\omega} + \delta\tilde{\omega}$, and one obtains the quantity $\tilde{\Phi} + \delta\tilde{\Phi}$. To the first order in variations, one gets

$$\delta\tilde{\Phi} = i \int_{V_c} [\tilde{\omega}(\mathbf{H}^* \cdot \delta\mathbf{B} + \mathbf{B} \cdot \delta\mathbf{H}^*) - \tilde{\omega}^*(\mathbf{E} \cdot \delta\mathbf{D}^* + \mathbf{D}^* \cdot \delta\mathbf{E}) + \delta\tilde{\omega} \mathbf{H}^* \cdot \mathbf{B} - \delta\tilde{\omega}^* \mathbf{E} \cdot \mathbf{D}^*] dV. \quad (3)$$

It is sufficient for the perturbation method to yield satisfactory results that $\delta\tilde{\Phi} \approx 0$, i.e., the quantity $\tilde{\Phi}$ as defined in Eq. (1) is practically unchanged. This implies that only the fields at the surface S_c of the cavity walls should remain unchanged. The fields in the sample may be varied significantly. These conditions can be met if the sample is small compared to the cavity and placed far from the cavity walls, e.g., in the interior of the cavity.

Equation (3) contains the complex frequency shift $\delta\tilde{\omega}$ which we want to evaluate, but it also involves its complex conjugate $\delta\tilde{\omega}^*$ so that a direct evaluation is impossible. By adapting the method of Kahan¹⁶ we calculate³⁷

$$\begin{aligned} 2i \int_{V_c} \text{Im}[\nabla \cdot (\mathbf{E}^* \times \delta\mathbf{H})] dV \\ = i \int_{V_c} [\tilde{\omega}(\mathbf{B} \cdot \delta\mathbf{H}^* - \mathbf{E}^* \cdot \delta\mathbf{D}) + \tilde{\omega}^*(\mathbf{B}^* \cdot \delta\mathbf{H} - \mathbf{E} \cdot \delta\mathbf{D}^*) \\ - \delta\tilde{\omega} \mathbf{E}^* \cdot \mathbf{D} - \delta\tilde{\omega}^* \mathbf{E} \cdot \mathbf{D}^*] dV. \end{aligned} \quad (4)$$

The left hand side of Eq. (4) vanishes under the above stated perturbation condition. Hence, by subtracting Eq. (4) from Eq. (3) one eliminates $\delta\tilde{\omega}^*$, and the complex frequency shift can be evaluated explicitly

$$\delta\tilde{\omega} = - \frac{\int_{V_c} [\tilde{\omega}(\mathbf{H}^* \cdot \delta\mathbf{B} + \mathbf{E}^* \cdot \delta\mathbf{D}) - \tilde{\omega}^*(\mathbf{B}^* \cdot \delta\mathbf{H} + \mathbf{D}^* \cdot \delta\mathbf{E})] dV}{\int_{V_c} (\mathbf{H}^* \cdot \mathbf{B} + \mathbf{E}^* \cdot \mathbf{D}) dV}, \quad (5)$$

where the integral in the denominator represents the energy stored in the cavity volume V_c and will be from now on denoted by W_c . The integration in the numerator of Eq. (5) needs to be taken only within the sample volume V_s where the properties of the material have changed. Outside the sample one assumes that $\mathbf{B} = \mu_0 \mathbf{H}$ and $\mathbf{D} = \epsilon_0 \mathbf{E}$ so that the terms cancel with the approximation $\tilde{\omega} \approx \tilde{\omega}^* \approx \omega$, which holds for high Q -factor values. In practical applications one keeps the input microwave power constant. The stored energy W_c then varies if the dissipation is changed. However, for large Q -factor values this effect can be neglected and one may consider W_c as constant.

Alternatively, one may carry out the calculation in terms of the surface integral and get the result³⁷

$$\delta\tilde{\omega} = \frac{i}{W_c} \oint_{S_s} (\mathbf{E}^* \times \delta\mathbf{H} - \mathbf{H}^* \times \delta\mathbf{E}) \cdot \mathbf{n}_s dS, \quad (6)$$

where the unit vector \mathbf{n}_s is perpendicular to the sample surface S_s and points into the sample. The approximation used in deriving Eq. (6) is that the filling factor $\Gamma = W_s/W_c$ is very small. It is readily achieved if the sample volume is much smaller than the cavity volume.

III. DEPOLARIZATION IN AC FIELDS

The depolarization phenomena are well known in the case of dielectric ellipsoids placed in a homogeneous dc electric field E_0 . The internal field becomes³⁰

$$E_i = E_0 - N \frac{P_i}{\epsilon_0} = \frac{E_0}{1 + (\epsilon_r - 1)N}, \quad (7)$$

where N is the depolarization factor and ϵ_r is the relative permittivity of the dielectric. The problem of a dielectric or conducting sample in an ac electric field requires the solutions of a Helmholtz differential equation³¹ for the fields E and H inside and outside of the sample supplemented with the appropriate boundary conditions. For an ellipsoid, the solution is given in terms of a series of ellipsoidal harmonics.^{32,33} However, with such a solution the calculation of the complex frequency shift becomes intractable. Klein *et al.*²⁰ have treated a simpler case of a sphere and found that the complex frequency shift could be found in the quasistatic limit with an effective complex dielectric permittivity $\tilde{\epsilon}_{\text{eff}}$ which depends on the parameter $\tilde{k}a$, where \tilde{k} is the complex wave vector in the sample and a is the radius of the sphere. In the limit $|\tilde{k}a| \ll 1$, their result reduces to the Shchegolev form.²³ This is the depolarization regime in which the internal field E_i is practically homogeneous throughout the sample and close to the value of the driving field E_0 . At higher conductivities, however, when $|\tilde{k}a| \approx 1$, the solution with $\tilde{\epsilon}_{\text{eff}}$ predicts a significant deviation from that of Shchegolev. In particular, for $|\tilde{k}a| \gg 1$ it predicts correctly the result of the skin depth regime while the Shchegolev form fails to do so.

A compact analytical solution for platelike samples is most needed since high-temperature superconductors are usually prepared as platelike single crystals or thin films. In such cases, the field solutions for a slab geometry^{28,34–37} may serve as a good approximation

$$\tilde{E}(z) = \tilde{E} \left(\frac{d}{2} \right) \frac{\cosh(i\tilde{k}z)}{\cosh(i\tilde{k}d/2)}, \quad (8)$$

$$\tilde{B}(z) = \frac{1}{i\omega} \frac{\partial \tilde{E}(z)}{\partial z} = \frac{\tilde{k}}{\omega} \tilde{E} \left(\frac{d}{2} \right) \frac{\sinh(i\tilde{k}z)}{\cosh(i\tilde{k}d/2)}, \quad (9)$$

where d is the thickness of the slab and the z axis is taken perpendicular to the slab. The complex wave vector in a general material is given by

$$\tilde{k} = k_0 \sqrt{\tilde{\mu}_r \left(\tilde{\epsilon}_r - i \frac{\tilde{\sigma}}{\epsilon_0 \omega} \right)}, \quad (10)$$

where $k_0 = \omega \sqrt{\mu_0 \epsilon_0}$ is the vacuum wave vector and $\tilde{\mu}_r$, $\tilde{\epsilon}_r$, and $\tilde{\sigma}$ are the material parameters.

The question is how should the field $\tilde{E}(d/2)$ be related to the driving ac field E_0 . Schaumburg and Helberg^{34–36} have proposed to set the complex frequency shift calculated using the field $\tilde{E}(z)$ of Eq. (8) equal to that given by the Shchegolev formula. Here we adopt a different approach where we consider the surface problem of a flat ellipsoid which approximates our platelike sample. In response to the driving ac field E_0 , the sample will build charges on its surfaces.²⁸ Looking from the outside, the problem appears equivalent to

a quasistatic response of a fictitious substitute sample of the same size as the original one, but having some relative permittivity $\tilde{\epsilon}_s$. One can now relate the homogeneous electric field \tilde{E}_s in the substitute sample to the driving external field E_0 in analogy to the static case

$$\tilde{E}_s = \frac{E_0}{1 + (\tilde{\epsilon}_s - 1)N}. \quad (11)$$

The complex valued $\tilde{\epsilon}_s$ allows for a possible phase shift of \tilde{E}_s with respect to the driving ac field E_0 whose phase we take as zero. If the fields should look the same from outside the two samples, we have to equate the fields at their respective surfaces

$$\tilde{E}_s = \tilde{E} \left(\frac{d}{2} \right), \quad (12)$$

$$\tilde{H}_s = \tilde{H} \left(\frac{d}{2} \right). \quad (13)$$

Since the field \tilde{D}_s is also homogeneous, one finds the magnetic field at the surface

$$\tilde{H}_s = i\omega \tilde{D}_s \frac{d}{2} = i\omega \tilde{\epsilon}_s \epsilon_0 \tilde{E}_s \frac{d}{2}. \quad (14)$$

Using Eqs. (9) and (14) in Eq. (13) one finds

$$\tilde{\epsilon}_s = \frac{\tilde{k}^2}{\tilde{\mu}_r k_0^2} \frac{\tanh(i\tilde{k}d/2)}{i\tilde{k}d/2}. \quad (15)$$

The fictitious substitute sample was only used to relate the fields at the surface to the driving field E_0 . The fields inside the actual sample are given by Eqs. (8) and (9) with $\tilde{E}(d/2)$ replaced by \tilde{E}_s of Eq. (11). Applying these fields one may calculate the complex frequency shift given by either the volume integral in Eq. (5) or the surface integral in Eq. (6). This task will be postponed to the next section.

At this point it is useful to analyze some features of the fields at the surface of the sample which depend on the geometric factors N and d , when the parameters of the sample are varied. For an illustration we take only the case of a nonmagnetic ($\tilde{\mu}_r = 1$) and nondielectric ($\tilde{\epsilon}_r = 1$) normal conductor ($\tilde{\sigma} = \sigma_n$). In Fig. 2 we plot the amplitude and phase of $\tilde{E}(d/2)/E_0$, and $\tilde{B}(d/2)/E_0$ as functions of σ_n . A typical microwave frequency of $\omega/2\pi = 10$ GHz was used in the numerical calculations. The film thickness was chosen to be $d = 100$ nm, and the depolarization factor $N = 10^{-6}$. In the limit of negligible σ_n , i.e., $(\sigma_n/\epsilon_0\omega) \ll 1$, the fields are practically those of the electromagnetic mode in an empty cavity. Since the thickness of the film is much smaller than the vacuum wavelength ($d \ll \lambda_0$), the electric field at $d/2$ is practically at the maximum, and the magnetic field is extremely small. The magnetic field leads in phase by $\pi/2$ as required in a cavity mode. When σ_n is increased so that $(\sigma_n/\epsilon_0\omega) \approx 1$, the induced current $\tilde{J} = \sigma_n \tilde{E}$ becomes comparable to the

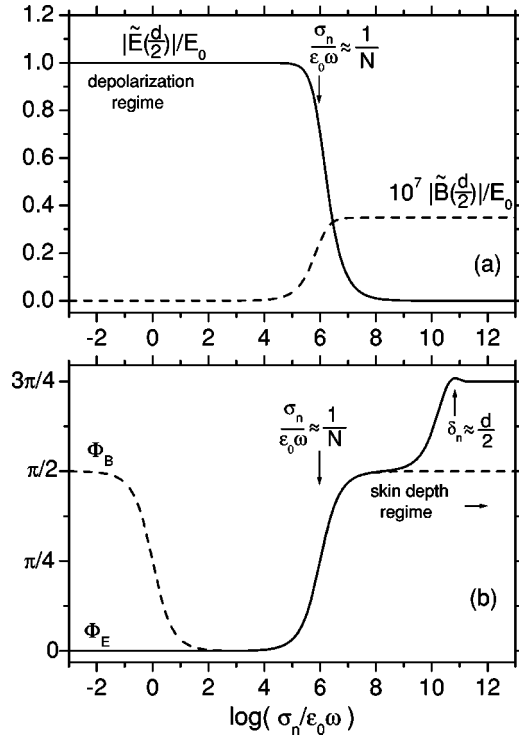


FIG. 2. Modulus (a) and phase (b) of the microwave electric and magnetic fields at the sample surface normalized to the driving field E_0 whose phase is taken as zero. With increasing conductivity of the sample one can trace the evolution from the depolarization regime to the skin depth regime. The geometric parameters of the sample are $N=10^{-6}$ and $d=100$ nm.

displacement current $i\epsilon_0\omega\tilde{E}$, and the sample starts to act as a conductor. This transition is reflected in the phase change of the magnetic field so that it gets in phase with the electric field.

At even higher conductivities one reaches the condition $(\sigma_n/\epsilon_0\omega) \approx N^{-1}$. By inspection of Eq. (11) one can realize that \tilde{E}_s will drop in amplitude and change phase with respect to the driving field E_0 . This is the *depolarization crossover* which is clearly depicted in Fig. 2. Physically, one may well understand this process by considering the effect of the charges built on the surface of the sample. In passing above the depolarization crossover, the surface charge density is increased so that the driving electric field E_0 is screened inside the sample. Under those conditions, the electric field found in the sample is related to the current $\tilde{J}=\sigma_n\tilde{E}$ which builds the surface charge density. The phase relationships are simple. The surface charge density always oscillates in phase with the driving field E_0 , and the current density \tilde{J} leads in phase by $\pi/2$ over the surface charge density. Hence, above the depolarization crossover the electric field \tilde{E} in the sample also leads in phase by $\pi/2$ over the driving field E_0 . As for the magnetic field, it increases in the depolarization crossover due to the current rise. Its phase follows that of the current and the electric field.

With the values of d chosen in the case presented in Fig. 2, the quantity $\tilde{k}d/2$ is still very small at the depolarization

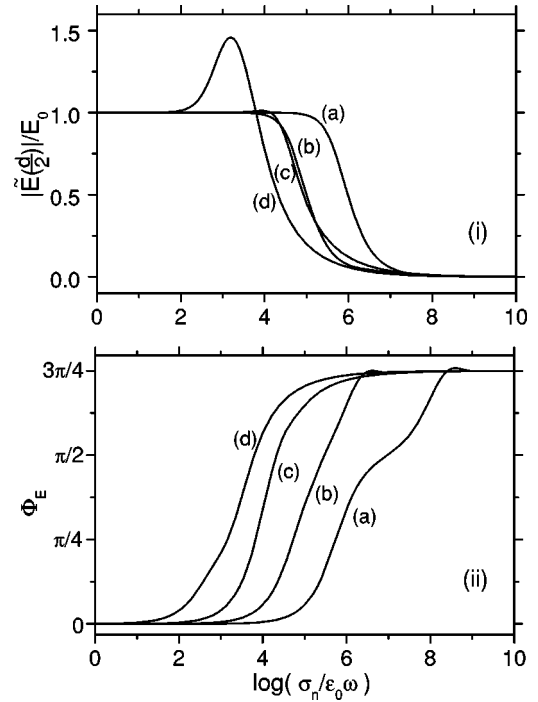


FIG. 3. Modulus (i) and phase (ii) of the microwave electric field at the surface of the samples with geometric parameters: (a) $N=10^{-6}$, $d=1$ μm , (b) $N=10^{-5}$, $d=10$ μm , (c) $N=7\times 10^{-5}$, $d=0.1$ mm, and (d) $N=7\times 10^{-4}$, $d=0.5$ mm.

crossover and slightly above it. This implies that one has $[\tanh(\tilde{k}d/2)]/(i\tilde{k}d/2) \approx 1$ in Eq. (15). Hence, the position of the depolarization crossover depends, in this case, solely on the value of N . Only at very high conductivities when $\tilde{k}d/2$ becomes comparable to unity, one observes a crossover to the skin depth regime. There, the amplitudes of the fields do not change appreciably, only the phase of the electric field takes a lead of $\pi/4$ over the magnetic field. In the limit of infinite conductivities, the electric field amplitude decreases to zero value and the magnetic field attains its maximum. Those are the perfect conductor conditions.

In Fig. 3 we present the calculation for thicker samples. The depolarizing factor generally increases for thicker samples, but its value depends also on the length and width of the sample. One could choose a number of combinations of d and N , but here we select only a few in order to illustrate an interesting feature. The curves in Fig. 3 are for samples of 1 μm , 10 μm , 0.1 mm, and 0.5 mm thickness with depolarization factors of 10^{-6} , 10^{-5} , 7×10^{-5} , and 7×10^{-4} , respectively. Figures 2 and 3 present the evolution of the curve shapes which have to be analyzed. The depolarization crossover shifts to lower conductivities linearly with N^{-1} . However, the skin depth crossover is determined by the condition $\delta_n \approx d/2$, where $\delta_n = \sqrt{2/\mu_0\omega\sigma_n}$ is the skin depth. Hence, a change of d by one order of magnitude shifts the skin depth crossover by two orders of magnitude on the conductivity scale. For samples close to 0.1 mm thickness, the two crossover regimes overlap, and, for even thicker samples, the skin depth regime precedes the depolarization crossover. These features are clearly seen in the phase of the electric field

shown in Fig. 3. It is also interesting to observe that the amplitude of the electric field exerts a pronounced maximum at the skin depth crossover in thick samples with low conductivities [cf. curve (d) in Fig. 3].

In practice, the samples can change their conductivities with temperature in a finite range. Good metallic conductors will cover only a range of high σ_n . If the sample is thick, one may observe only the skin depth regime. For thin metallic films, one could explore the region between the tail of the depolarization crossover and the onset of the skin depth regime. Eventually for very thin films one may observe the depolarization crossover. With low-conductivity semiconductors, one may achieve the cases in which the two crossover regimes overlap. Such cases will be shown experimentally in Sec. VI.

IV. COMPLEX FREQUENCY SHIFT

Using the fields of the preceding section it is straightforward to calculate the complex frequency shift induced by a change of the conductivity of the sample. The starting conductivity defines the initial state of the system, and the altered conductivity the final one. From the surface integral of Eq. (6) one finds after a straightforward calculation

$$\frac{\Delta \tilde{\omega}_{fi}}{\omega} = \frac{\Gamma}{N} \left[\frac{1}{1 + (\tilde{\epsilon}_{sf} - 1)N} - \frac{1}{1 + (\tilde{\epsilon}_{si} - 1)N} \right], \quad (16)$$

where $\tilde{\epsilon}_{si}$ and $\tilde{\epsilon}_{sf}$ stand for the initial and final states, respectively. We denoted by Γ the dimensionless filling factor of the sample in the cavity

$$\Gamma = \frac{\epsilon_0 E_0^2 V_s}{W_c}, \quad (17)$$

where V_s is the sample volume. In deriving Eq. (16) we used the approximation $\omega_f \approx \omega_i \approx \omega$ in the expressions for the magnetic fields in Eq. (6), and the surface integration was made within the slab geometry approximation on the two surfaces of area V_s/d .

The same result of Eq. (16) can be obtained from the volume integration given by Eq. (5). There, one has to use for the fields $\tilde{E}(z)$ and $\tilde{B}(z)$ the expressions given by Eqs. (8) and (9), while $\tilde{D} = \tilde{\epsilon}_s \epsilon_0 \tilde{E}_s$ is taken as homogeneous, and, correspondingly, $\tilde{H}(z) = i\omega \tilde{D}z$ with a linear space dependence. Note that even though the sample is assumed to be in the node of the empty cavity magnetic field, the magnetic terms in Eq. (5) should not be disregarded in favor of the electric terms. In fact, some of the magnetic terms cancel with the electric terms, and the result of Eq. (16) is obtained.

One can verify that the function $1/[1 + (\tilde{\epsilon}_s - 1)N]$ is analytical in the complex $\tilde{\sigma}$ plane. Hence, its total differential determines an infinitesimal shift and the total shift between any two states does not depend on the integration path.

It is useful to take the perfect conductor as the initial state. The second term in Eq. (16) then vanishes, and one obtains for the complex frequency shift from the perfect conductor to an arbitrary state³⁷

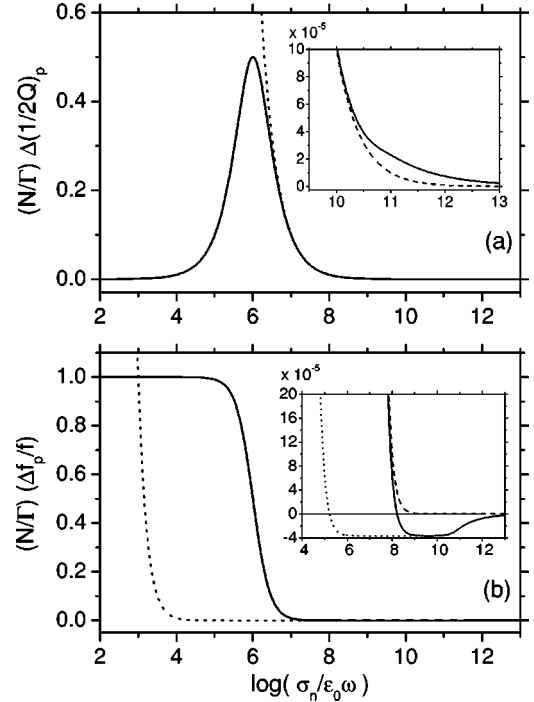


FIG. 4. Real and imaginary parts of the complex frequency shift calculated by the general formula of Eq. (18) (solid lines), Shchegolev formula (dashed lines), and Eq. (19) (dotted lines). The geometric parameters of the sample are the same as in Fig. 2. The dashed line in (a) is indistinguishable from the solid line over the whole depolarization peak. At high conductivities shown in the inset of (a), the dotted line is indistinguishable from the solid line.

$$\frac{\Delta \tilde{\omega}_p}{\omega} = \frac{\Gamma}{N} \left[1 + \left(\frac{\tilde{k}^2 \tanh(i\tilde{k}d/2)}{k_0^2 i\tilde{k}d/2} - 1 \right) N \right]^{-1}, \quad (18)$$

where we have used the explicit form for $\tilde{\epsilon}_s$ of a nonmagnetic conductor.

It is easy to verify that in the limit of low conductivities, i.e., for small values of $\tilde{k}d/2$, Eq. (18) is reduced to the expression given by Shchegolev²³ with an offset of Γ/N when the complex frequency shift is evaluated from the empty cavity state. In the other limit of very high conductivities, Eq. (18) becomes approximately

$$\frac{\Delta \tilde{\omega}_p}{\omega} \approx - \frac{\Gamma}{N^2} \frac{k_0^2 d/2}{i\tilde{k}} \coth(i\tilde{k}d/2), \quad (19)$$

which is identical to our previous result.²⁸ Thus, the result in Eq. (18) is a general solution for the full range of conductivities from zero to infinity. In Fig. 4 we plot the real and imaginary parts of the complex frequency shift for a sample with $N = 10^{-6}$ and $d = 100$ nm, which are the same geometric parameters as in Fig. 2. The full line represents the calculation based on Eq. (18), while dashed and dotted lines represent the Shchegolev approximation and the approximation given by Eq. (19), respectively. One can clearly see that, in this example, the Shchegolev expression is satisfactory not only in the depolarization regime, as expected, but also through the entire depolarization crossover and slightly

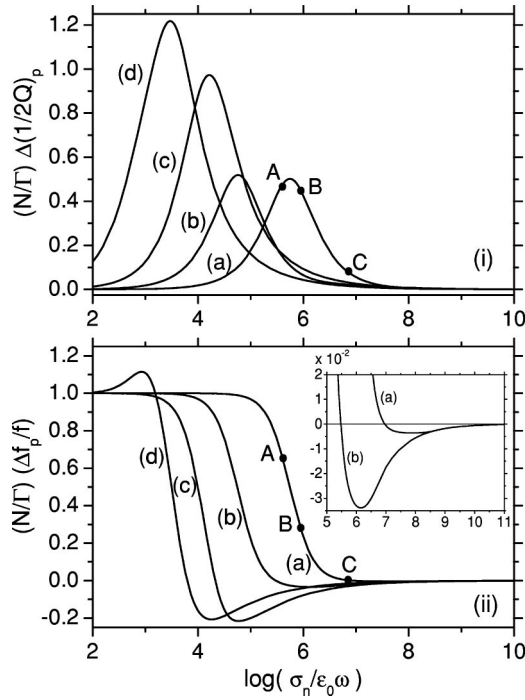


FIG. 5. Real and imaginary parts of the complex frequency shift calculated by Eq. (18) for the samples with geometric parameters as in Fig. 3. The points A, B, and C have σ_n coordinates which are assumed for $\sigma_n(T_c)$ values in the calculation of the corresponding curves in Fig. 7.

above. It deviates from the general solution of Eq. (18) at conductivities which are fairly above the depolarization crossover but still much below the skin depth crossover. In that region, the Shchegolev expression underestimates the absorption given by $\Delta(1/2Q)$. It also predicts that the frequency shift $\Delta f/f$ never changes sign, i.e., it approaches the perfect-conductor limit from above, which is in contrast to the well known behavior in the skin depth regime. The approximate expression in Eq. (19) is seen to yield satisfactory result in the skin depth regime and in a limited range of conductivities below it. However, as the depolarization crossover is approached, Eq. (19) becomes invalid.

It is interesting to follow the complex frequency shift for a set of samples of different N and d as in Fig. 3 where the electric field was analyzed. Figure 5 shows the curves calculated by Eq. (18). The curves are normalized by Γ/N in order to be presented on the same scale. The most interesting feature is the change of the shape of the calculated $\Delta f/f$ curve for thicker samples. This characteristic shape could never be obtained by the Shchegolev expression which contains only N , but not d . Therefore, the curves calculated by the Shchegolev expression always have the same shape and are merely displaced along the conductivity axis for different values of N . Equation (18) on the contrary depends on both N and d and can yield curves of different shapes. The negative plateau in $\Delta f/f$, which is well seen for the thin sample in Fig. 4, is still discernible for sample (a) in the inset of Fig. 5. However, for thicker samples it evolves into a pronounced minimum. Finally, a signal shape, which is very much different

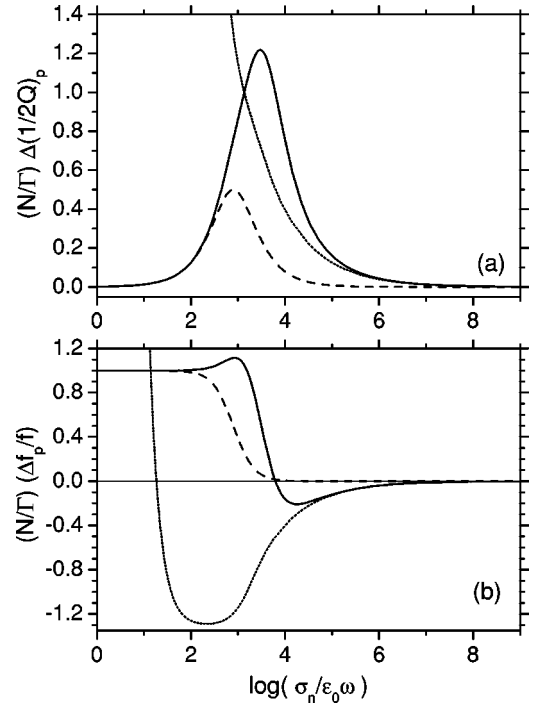


FIG. 6. Real and imaginary parts of the complex frequency shift for the sample with geometric parameters as in the case (d) of Fig. 5. The calculations were made by the general formula of Eq. (18) (solid lines), Shchegolev formula (dashed lines), and Eq. (19) (dotted lines).

from that of Shchegolev, appears for sample (d). An experimental illustration of such a case will be given in Sec. VI.

The range of the validity of the Shchegolev expression shown in Fig. 4 for a thin sample is not universal. For the thicker samples shown in Fig. 5, the Shchegolev expression gradually reduces its range of validity to lower conductivities. In particular, for the sample with $d=0.5$ mm and $N=7 \times 10^{-4}$ [the same as case (d) in Fig. 5], one finds that the Shchegolev expression agrees with the general solution given by Eq. (18) only below the depolarization crossover. Figure 6 shows the calculated curves. The approximate expression given by Eq. (19) preserves its validity above the depolarization crossover, even in this geometry. One can see that over the entire depolarization crossover none of the approximate solutions is acceptable.

It is interesting to analyze some cases of superconducting thin films. We shall illustrate these cases by keeping the film thickness $d=100$ nm and the depolarization factor $N=10^{-6}$ as for the sample in Fig. 4, and assume that the hypothetical materials could have some selected values for $\sigma_n(T_c)$. For the purpose of numerical simulations of the complex frequency shift, we assume the temperature dependence of the normal state conductivity $\sigma_n(T)=\sigma_n(T_c)/(a+bT/T_c)$ with $a=0.1$ and $b=0.9$. In the superconducting state, we assume the two-fluid conductivity $\tilde{\sigma}=\sigma_1-i\sigma_2$ with $\sigma_1=\sigma_n(T_c)(T/T_c)^4$ and $\sigma_2=K\sigma_n(T_c)[1-(T/T_c)^4]$, where $K=\sigma_2(0)/\sigma_n(T_c)$ is the ratio which we choose to be 20. Figure 7 shows the real and imaginary parts of the complex frequency shift in three cases selected by different val-

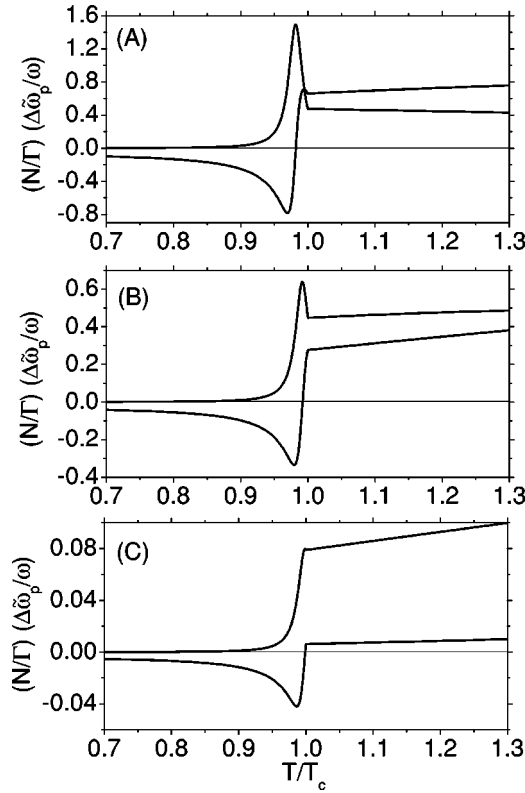


FIG. 7. Temperature dependences of the complex frequency shift calculated by Eq. (18) for the sample with geometric parameters as in the case (a) of Fig. 5. The assumed conductivities in the normal and superconducting states are described in the text. The values of $\sigma_n(T_c)$ in the cases (A), (B), and (C) are the same as for the points A, B, and C in Fig. 5.

ues of $\sigma_n(T_c)$. For the case labeled (A), the conductivity $\sigma_n(T_c)$ is low enough that this point is below the depolarization peak (see Fig. 5). One may look at the curves as if the sample were cooled from above T_c to lower temperatures. In the normal state the metallic conductivity increases as the sample is cooled. Hence, when point A in Fig. 5 is approached from below, one should obtain an increase of $\Delta(1/2Q)$ and a decrease of $\Delta f/f$. This, indeed, is observed in case (A) of Fig. 7 when T_c is approached from above. Below the superconducting transition, one observes first a peak in $1/2Q$ followed by a drop to zero at lower temperatures. The frequency shift $\Delta f/f$ for case (A) in Fig. 7 drops from relatively high value at T_c (see point A in Fig. 5), crosses the zero level, exerts a minimum, and then saturates at a negative value for low temperatures. It can be seen from Eq. (18) that the low-temperature value of $\Delta f/f$ must always be negative, i.e., a superconductor at $T=0$ has a negative frequency shift with respect to the perfect conductor. This occurs since the penetration depth vanishes in the perfect conductor limit, but in a superconductor it saturates to $\lambda_L(0)$.

In the case labeled (B) in Fig. 7, the conductivity $\sigma_n(T_c)$ is chosen to be higher so that the sample is above the depolarization peak. If point B in Fig. 5 is approached from lower conductivities, one should observe a decrease in $\Delta(1/2Q)$. This is now seen in case (B) of Fig. 7 when the sample is

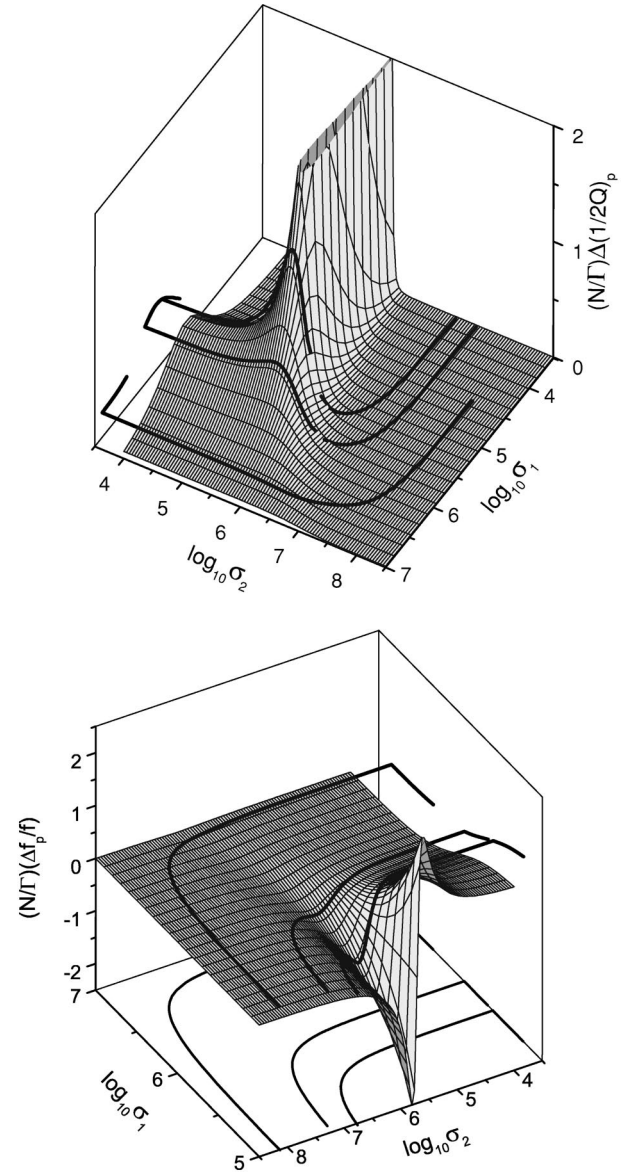


FIG. 8. 3D plots of the complex frequency shift calculated by Eq. (18) for the sample with geometric parameters as in Fig. 7. The three paths in the complex $\tilde{\sigma}$ plane correspond to those assumed for cases (A), (B), and (C) in Fig. 7.

cooled from above T_c . If the temperature scale were extended very much above T_c , the curve of $\Delta(1/2Q)$ would exhibit a maximum, i.e., the depolarization peak would be crossed.

Finally, case (C) in Fig. 7 shows $\Delta(1/2Q)$ and $\Delta f/f$ calculated for a film whose $\sigma_n(T_c)$ is on the upper tail of the depolarization crossover (see point C in Fig. 5). For $T > T_c$, the slope of $\Delta f/f$ has become smaller than that of $\Delta(1/2Q)$. Also, one may observe that the level of $\Delta f/f$ at T_c is not much above the low-temperature value. The curve for $\Delta(1/2Q)$ drops rapidly to zero, i.e., without showing any peak just below T_c .

One could select a number of other values of $\sigma_n(T_c)$ and show minor variations of the cases shown in Fig. 7. Rather than showing the results of such calculations, we find it in-

teresting to look at a 3D plot of $\Delta(1/2Q)$ and $\Delta f/f$ over the complex $\tilde{\sigma}$ plane. Figure 8 shows such graphs for the sample of the same geometry as used in Fig. 7. The three pathways indicated in Fig. 8 are those taken for the temperature dependences of the conductivities in the normal and superconducting states for the cases (A), (B), and (C) in Fig. 7. Those pathways trace the assumed two-fluid conductivities. The true complex conductivity $\tilde{\sigma}(T) = \sigma_1(T) - i\sigma_2(T)$ in a given material would trace its own path in Fig. 8. Thus, the temperature dependences of $\Delta(1/2Q)$ and $\Delta f/f$ may take different shapes. It is the task of an inversion procedure to extract $\sigma_1(T)$ and $\sigma_2(T)$ from experimentally measured values of $\Delta(1/2Q)$ and $\Delta f/f$.

The 3D plot shown in Fig. 8 is made for a given geometry of the sample. Different paths on this plot may represent various superconducting materials. In another approach, one could consider a given material being cut into samples of different geometries. Obviously, for a given material, the path in the complex plane is always given by the same $\sigma_1(T)$ and $\sigma_2(T)$. However, each sample may have a different depolarization factor N so that the corresponding 3D plots of the complex frequency shift appear with displaced characteristic peaks and minima. With the same path in the complex $\tilde{\sigma}$ plane, the observed experimental curves may have different shapes. However, in a correct analysis of those apparently different experimental signals one should obtain the same intrinsic $\sigma_1(T)$ and $\sigma_2(T)$.

V. THE ROLE OF DIELECTRIC SUBSTRATES

Superconducting thin films are usually grown on dielectric substrates which have relatively large permittivities ϵ_r , ranging from 10 to 25.³⁸ When placed in the microwave cavity, such samples are not expected to act as pure thin films since the presence of the dielectric on one side of the film introduces an asymmetry. Rather than attempting a complicated field solution for this composite structure, we merely note the global effect and try to mimic it by a simple asymmetric solution. The external field E_0 drives also the displacement current $\partial\tilde{D}/\partial t$ in the dielectric substrate. Hence, the magnetic field is produced by both the current in the thin film and the displacement current in the dielectric substrate. Therefore, the node of the magnetic field is not found in the center of the thin film, but displaced by some amount ζ from it. Disregarding the actual fields in the substrate, we may write for the fields in the conducting film

$$\tilde{E}(z) = \tilde{E}_s \frac{\cosh[i\tilde{k}(z - \zeta)]}{\cosh[i\tilde{k}(d/2 + \zeta)]}, \quad (20)$$

$$\tilde{B}(z) = \frac{1}{i\omega} \frac{\partial \tilde{E}(z)}{\partial z} = \frac{\tilde{k}}{\omega} \tilde{E}_s \frac{\sinh[i\tilde{k}(z - \zeta)]}{\cosh[i\tilde{k}(d/2 + \zeta)]}. \quad (21)$$

We may apply the concept of a fictitious substitute sample as in Sec. III. In the present case, the substitute sample should be centered at $z = \zeta$ and have the thickness $2\zeta + d$ in order that the fields in this sample are symmetric about its center. Equation (14) can now be replaced by the condition

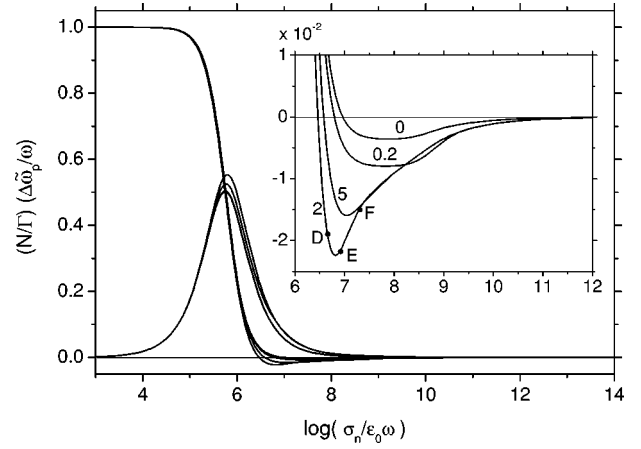


FIG. 9. Complex frequency shift calculated by Eq. (24) for the sample with geometric parameters as in the case (a) of Fig. 5. The asymmetry ratio ζ/d is indicated as a number. The points D, E, and F have σ_n coordinates which are assumed for $\sigma_n(T_c)$ values in the calculation of the corresponding curves in Fig. 11.

$$\tilde{H}(d/2) - \tilde{H}(-d/2) = i\omega \tilde{D}_s d = i\omega \tilde{\epsilon}_s \epsilon_0 \tilde{E}_s d, \quad (22)$$

and the relative permittivity of the substitute sample becomes

$$\tilde{\epsilon}_s = \frac{\tilde{k}^2}{k_0^2} \frac{1}{[\coth(i\tilde{k}d/2) + \tanh(i\tilde{k}\zeta)] i\tilde{k}d/2}. \quad (23)$$

The complex frequency shift is again calculated by Eq. (16) between the initial and final states. For the shift from perfect conductor one finds³⁷

$$\frac{\Delta \tilde{\omega}_p}{\omega} = \frac{\Gamma}{N} \left[1 + \left(\frac{\tilde{k}^2}{k_0^2} \frac{1}{[\coth(i\tilde{k}d/2) + \tanh(i\tilde{k}\zeta)] i\tilde{k}d/2} - 1 \right) N \right]^{-1}. \quad (24)$$

Obviously, for $\zeta \rightarrow 0$ this expression reduces to that of Eq. (18).

In Fig. 9 we plot the calculated complex frequency shift for $\zeta = 0, 0.2d, 0.5d, 2d$, and $5d$ in a sample of geometric parameters $d = 1 \mu\text{m}$ and $N = 10^{-6}$. The asymmetry produces a small increase of $\Delta(1/2Q)$ at and above the depolarization peak. The effect of asymmetry on $\Delta f/f$ is observed only in the upper tail of the depolarization crossover. The inset to Fig. 9 shows on an expanded scale the changes in $\Delta f/f$ with the asymmetry. For higher ratios of ζ/d , the curves of $\Delta f/f$ develop a pronounced minimum. This implies that the experimental curves of $\Delta f/f$, with σ_n increasing only in a limited range of values, may appear with either negative or positive slopes, or exhibit a minimum.

Asymmetry has a noticeable effect on the temperature dependences of the complex frequency shift. In Fig. 10 we plot $\Delta(1/2Q)$ and $\Delta f/f$ for $\zeta = 2d$ and $\zeta = 5d$ in the sample with geometric parameters as in Fig. 9. The conductivities in the normal and superconducting states were assumed to be the same as in the calculations of the preceding section. The case shown in Fig. 10 is for $\sigma_n(T_c)$ chosen to be smaller than that which yields the minimum in the frequency shift curves in

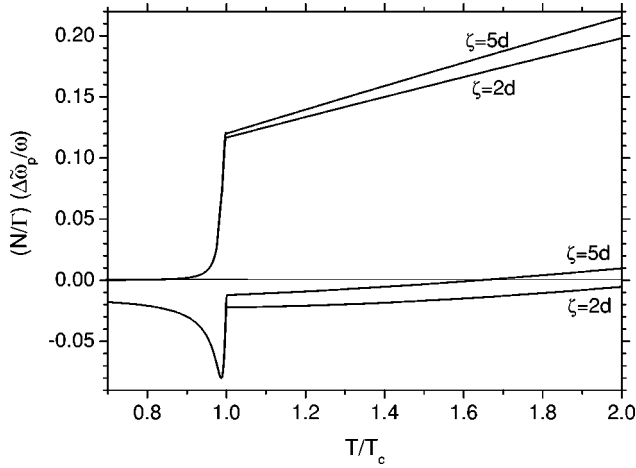


FIG. 10. Temperature dependences of the complex frequency shift calculated by Eq. (24) with asymmetry parameters $\zeta = 2d$ and $5d$. The geometric parameters of the thin film are the same as in Fig. 9.

Fig. 9. One can see that, in this case, the behavior of the complex frequency shift below T_c is not much affected by the change in the asymmetry parameter ζ . Above T_c , however, larger asymmetry brings about a bigger slope in $\Delta(1/2Q)$. The level of $\Delta f/f$ at T_c is increased above that observed at very low temperatures, and the slope at $T > T_c$ is also increased. These qualitative features will be demonstrated by experimental results in the next section.

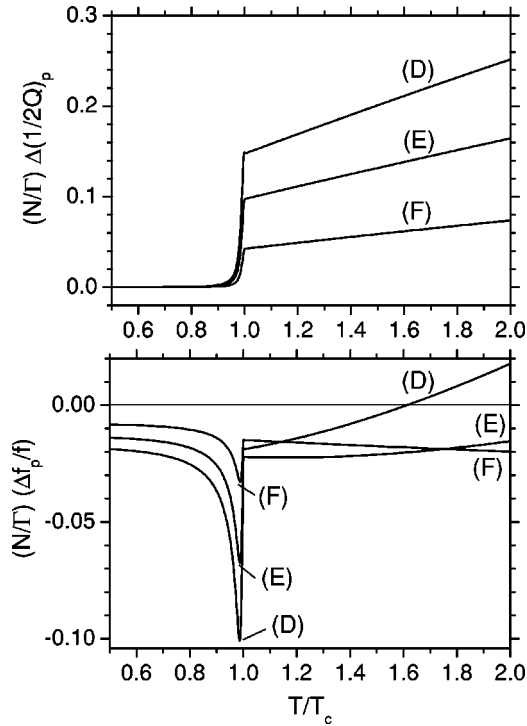


FIG. 11. Temperature dependences of the complex frequency shift calculated by Eq. (24) with asymmetry parameters $\zeta = 2d$. The geometric parameters of the thin film are the same as in Fig. 9. The values of $\sigma_n(T_c)$ in the cases (D), (E), and (F) are the same as for the points D, E, and F in Fig. 9.

Figure 11 shows the calculated complex frequency shift for some chosen values of $\sigma_n(T_c)$ in a sample with the same geometric parameters as in Figs. 9 and 10. The asymmetry parameter was chosen to be $\zeta = 2d$. The absolute values and slopes of $\Delta(1/2Q)$ at $T > T_c$ decrease for larger $\sigma_n(T_c)$. The interesting evolution is seen in the curves for $\Delta f/f$. When $\sigma_n(T_c)$ is chosen to be the same as for point D in the inset of Fig. 9, the slope of $\Delta f/f$ in Fig. 11 is positive above T_c . For $\sigma_n(T_c)$ as in point E in the inset of Fig. 9, the curve for $\Delta f/f$ in Fig. 11 passes through a minimum when the temperature is raised above T_c . Finally, for a still larger value of $\sigma_n(T_c)$, as in point F of the inset of Fig. 9, one observes only a negative slope for $\Delta f/f$ above T_c . We have observed such cases experimentally, and some examples will be presented in the next section.

VI. EXPERIMENTAL RESULTS

In the preceding sections we have shown that the general solution of the complex frequency shift of thin films in the electric component of the microwave field in a cavity predicts a number of interesting features. In this section we only present the experimental evidence for these features without entering into a detailed discussion of the electronic properties of the materials. The samples were measured in an elliptical copper cavity resonating in ${}_{\epsilon}\text{TE}_{111}$ mode at ≈ 9.5 GHz. The temperature of the sample could be varied from 2 K to room temperature by a heater and sensor assembly mounted on the sapphire sample holder. The Q factor was measured by a recently introduced modulation technique.^{39,40} The empty cavity had $1/2Q$ close to 20 ppm and this value is subtracted in all data shown in this section. Thus $\Delta(1/2Q)$ values in the experimental curves stand for the absorption caused by the sample itself. An automatic frequency control (AFC) system was used to lock the frequency of the source to the cavity resonance. The actual microwave frequency was monitored by a frequency counter.

Figure 12 shows the measured complex frequency shift of a doped Si sample of dimensions $4 \times 1.5 \times 0.5$ mm³ with a thin Nb film on one of its larger faces. The superconducting transition of Nb at 9 K is well observed. More interesting here is the complex frequency shift due to the doped Si. This material has $\epsilon_r \approx 12$ and a semiconducting behavior. As the sample is cooled below 100 K, the conductivity of doped Si decreases by orders of magnitude. Near 30 K, one observes the depolarization peak in $\Delta(1/2Q)$. The corresponding frequency shift $\Delta f/f$ shows the salient feature of a thick weakly conducting sample as theoretically predicted in curve (d) of Fig. 5.

Figure 13 gives an example of a thin BSCCO film where $\sigma_n(T_c)$ is slightly below the value required for the depolarization crossover. When the sample is cooled from 170 K, the observed $\Delta(1/2Q)$ increases. Below T_c (≈ 110 K), one observes first a sharp increase of $\Delta(1/2Q)$ followed by a rapid decrease at lower temperatures. The frequency shift $\Delta f/f$ is very high in the normal state and decreases upon cooling. Below T_c it drops dramatically to a minimum and then saturates at low temperatures. The main features of this signal are comprised in curve (A) of Fig. 7. Note that the

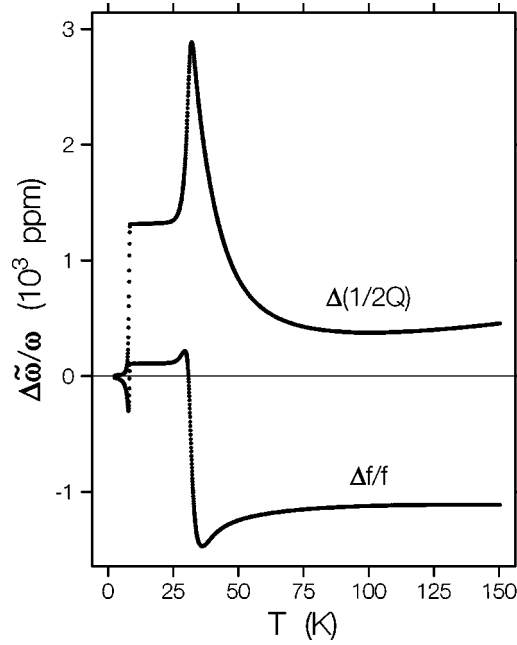


FIG. 12. Experimental complex frequency shift measured on a doped Si sample ($4 \times 1.5 \times 0.5 \text{ mm}^3$) with a Nb film on one of its larger faces.

experimental signal in Fig. 13 demonstrates pronounced roundings at T_c which indicate strong superconducting fluctuations in the BSCCO system. This fluctuation conductivity^{37,41} makes the detailed shape of the curves in Fig. 13 different from those in Fig. 7 which were calculated with the simple normal state and two-fluid conductivities.

An example of a thin film with high conductivity is shown in Fig. 14. It was a 10 nm thick Nb film on an Al_2O_3

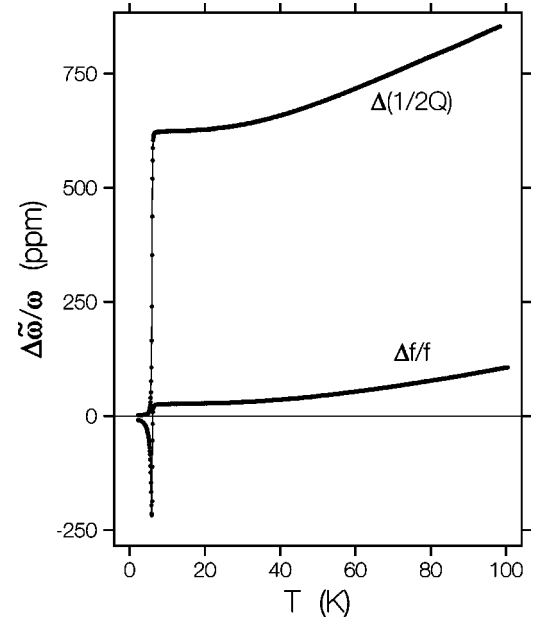


FIG. 14. Experimental complex frequency shift measured on a Nb film grown on Al_2O_3 substrate. The conductivity $\sigma_n(T_c)$ is much higher than that required for the depolarization crossover.

substrate.⁴⁰ The saturation of both $\Delta(1/2Q)$ and $\Delta f/f$ in the normal state below 30 K is due to the residual resistivity in this material. The overall shape of the curves is similar to case (C) in Fig. 7, i.e., to a film which is on the upper tail of the depolarization crossover.

A demonstration of the asymmetry played by the dielectric substrate is shown in Fig. 15. We measured a sample of a BSCCO thin film ($d = 500 \text{ nm}$) of length 3 mm and width

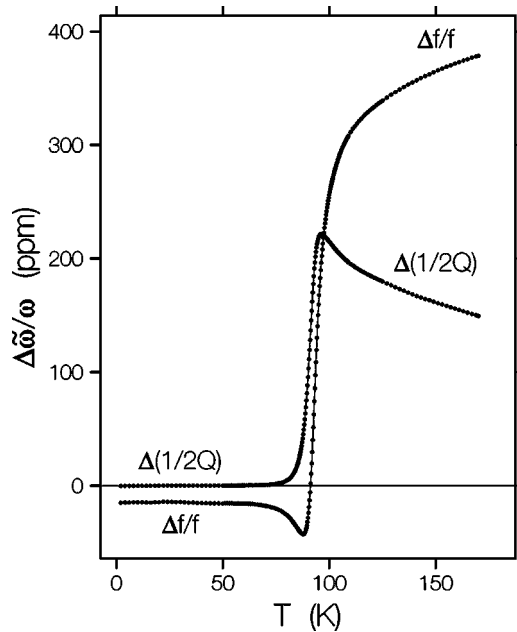


FIG. 13. Experimental complex frequency shift measured on a thin BSCCO film with $\sigma_n(T_c)$ below the value required for the depolarization crossover.

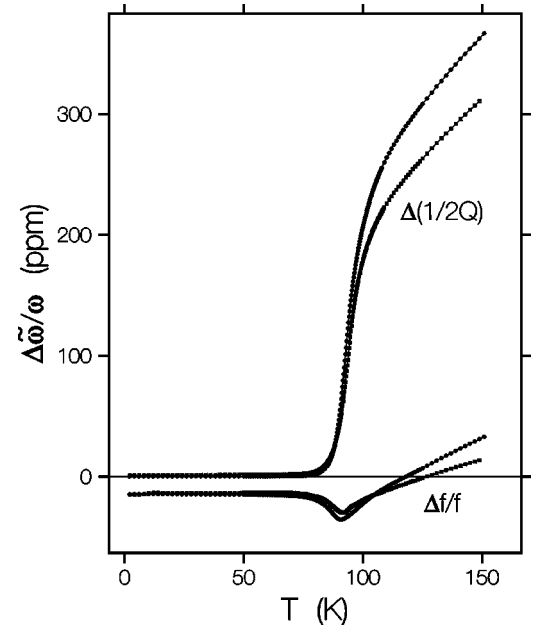


FIG. 15. Experimental complex frequency shift measured on a BSCCO thin film grown on a 1 mm thick LaAlO_3 substrate (higher slopes). The same piece was measured again after the substrate was grinded to 0.2 mm.

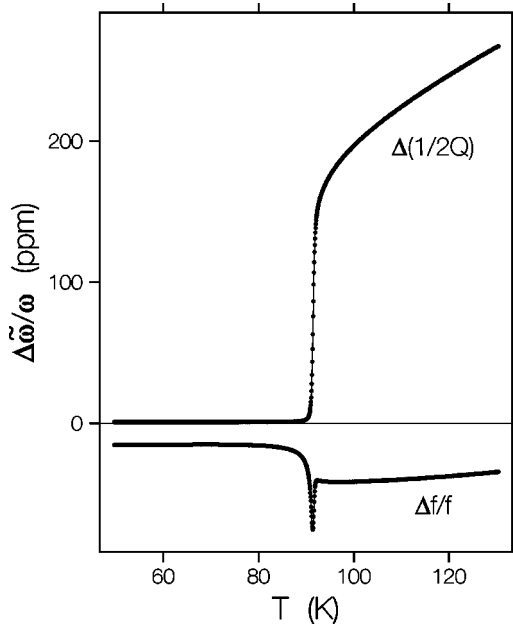


FIG. 16. Experimental complex frequency shift measured on an YBCO thin film grown on a 0.5 mm thick LaAlO_3 substrate. A minimum in $\Delta f/f$ is observed above T_c .

1 mm on a 1 mm thick LaAlO_3 substrate. The same sample was measured again after grinding the thickness of the substrate to 0.2 mm.³⁷ A thinner substrate obviously must bring about less asymmetry for the film. One can observe in Fig. 15 that lower asymmetry yields a smaller slope in $\Delta(1/2Q)$ above T_c . It also makes a smaller slope in $\Delta f/f$. Those are the main features observed also in the calculated signals in Fig. 10. Here, again, the fluctuations around T_c produce roundings in the experimental curves and change the detailed shapes of the curves.

Figure 16 shows experimental signals on an YBCO film ($d=400$ nm) on a 0.5 mm thick LaAlO_3 substrate.⁴⁰ The length of the film was 4 mm and the width 0.5 mm. This sample shows that a minimum in $\Delta f/f$ can occur above T_c even though there is no sign of an extremum in conductivity as seen from the $\Delta(1/2Q)$ curve. This is the case of $\sigma_n(T_c)$ being just above the value required for the minimum of $\Delta f/f$ (e.g., point E in the inset of Fig. 9). At higher temperatures the conductivity decreases and the frequency shift exhibits a minimum. A qualitatively similar feature was found in the calculated curve in Fig. 11.

Finally, Fig. 17 shows the complex frequency shift measured in a borocarbide film ($d=350$ nm) on an Al_2O_3 substrate.³⁷ The length of the film was 4 mm, the width 0.5 mm, and the substrate thickness was 1 mm. The curve for $\Delta(1/2Q)$ shows that the resistivity has a metallic behavior in the normal state. Below about 40 K one observes a gradual saturation due to the residual resistivity. The frequency shift $\Delta f/f$ exhibits a negative slope above T_c in the whole region of temperatures covered in the measurement. The conductivity $\sigma_n(T_c)$ is appreciably higher than that required for the minimum of $\Delta f/f$ (such as, e.g., point F in the inset of Fig. 9). For $T > T_c$, the conductivity is reduced, but not enough to reach the minimum of $\Delta f/f$ within the experimental range of

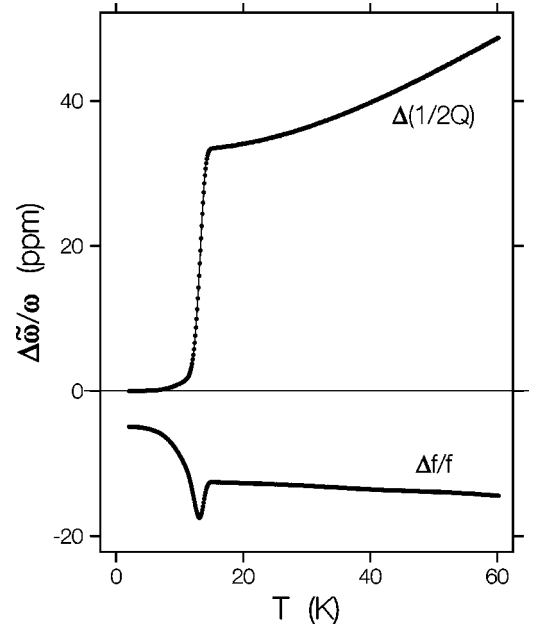


FIG. 17. Experimental complex frequency shift measured in borocarbide thin film on a Al_2O_3 substrate. A negative slope in $\Delta f/f$ is observed above T_c .

temperatures. Such a behavior is seen also in the calculated curve in Fig. 11.

VII. CONCLUSIONS

We have treated the problem of thin films in the microwave electric field maximum in a cavity in great detail. Our solution for the complex frequency shift is generally valid for all changes of the material parameters, i.e., dielectric ($\tilde{\epsilon}_r$), magnetic ($\tilde{\mu}_r$), and conducting ($\tilde{\sigma}$). It covers the full range of conductivity from zero to infinity, i.e., to the perfect conductor limit. We show that the previously known Shchegolev expression^{23,24,26} is the low-conductivity approximation of our solution. In the high-conductivity limit, the present solution yields the same behavior as we found earlier.²⁸

When applied to superconductor films, the present formula for the complex frequency shift may predict a diversity of signal shapes, depending on the geometric parameters of the sample and on its conductivity. A number of characteristic signal shapes are calculated using the present general formula and experimental demonstration of those diverse signal shapes is provided. The role of the dielectric substrate, on which the thin film is grown, is also considered. It is shown that to a good approximation the effect of the substrate can be accounted for by introducing an asymmetry parameter. Both calculations and experimental evidence are shown to support this role of the dielectric substrate. We expect that this analysis will help to investigate microwave absorption and frequency shift for a wide range of different samples with thin film geometry, ranging from metals, superconductors, semiconductors to magnetic, dielectric and even biological samples.

ACKNOWLEDGMENTS

D.-N. Peligrad and B. Nebendahl acknowledge support by the Deutsche Forschungsgemeinschaft (DFG) Project No.

Me362/14-1,2. A. Dulčić, M. Požek, and D. Paar acknowledge support from the Croatian Ministry of Science, DLR Stiftung (Project No. KRO-004-98).

*Present address: Philips Research Laboratories, Weisshausstrasse 2, D-52066, Aachen, Germany.

[†]To whom correspondence should be addressed.

Electronic address: dulcic@faust.irb.hr;

Electronic address: dragos.peligrad@philips.com

[‡]Present address: Agilent Technologies, Herrenberger Str. 130, D-71034, Böblingen, Germany.

¹N. Klein, N. Tellmann, H. Schulz, K. Urban, S. A. Wolf, and V. Z. Kresin, Phys. Rev. Lett. **71**, 3355 (1993).

²W. N. Hardy, D. A. Bonn, D. C. Morgan, R. Liang, and K. Zhang, Phys. Rev. Lett. **70**, 3999 (1993).

³D. A. Bonn, S. Kamal, K. Zhang, R. Liang, D. J. Baar, E. Klein, and W. N. Hardy, Phys. Rev. B **50**, 4051 (1994).

⁴S. Kamal, D. A. Bonn, N. Goldenfeld, P. J. Hirschfeld, R. Liang, and W. N. Hardy, Phys. Rev. Lett. **73**, 1845 (1994).

⁵T. Jacobs, S. Sridhar, Q. Li, G. D. Gu, and N. Koshizuka, Phys. Rev. Lett. **75**, 4516 (1995).

⁶H. Kitano, T. Shibauchi, K. Uchinokura, A. Maeda, H. Asaoka, and H. Takei, Phys. Rev. B **51**, 1401 (1995).

⁷S. M. Anlage, J. Mao, J. C. Booth, D. H. Wu, and J. L. Peng, Phys. Rev. B **53**, 2792 (1996).

⁸S.-F. Lee, D. C. Morgan, R. J. Ormeno, D. M. Broun, R. A. Doyle, J. R. Waldram, and K. Kadowaki, Phys. Rev. Lett. **77**, 735 (1996).

⁹H. Srikanth, B. A. Willemsen, T. Jacobs, S. Sridhar, A. Erb, E. Walker, and R. Flükiger, Phys. Rev. B **55**, R14 733 (1997).

¹⁰H. Kitano, T. Hanaguri, and A. Maeda, Phys. Rev. B **57**, 10 946 (1998).

¹¹D. Neri, E. Silva, S. Sarti, R. Marcon, M. Giura, R. Fastampa, and N. Sparvieri, Phys. Rev. B **58**, 14 581 (1998).

¹²J. R. Waldram, P. Theopistou, A. Porch, and H.-M. Cheach, Phys. Rev. B **59**, 1528 (1999).

¹³H. A. Bethe and J. Schwinger (unpublished).

¹⁴H. B. G. Casimir, Philips Res. Rep. **6**, 162 (1951).

¹⁵E. G. Spencer, R. C. LeCraw, and L. A. Ault, J. Appl. Phys. **28**, 130 (1957).

¹⁶E. Argenç and T. Kahan, *Theory of Waveguides and Cavity Resonators* (Balckie and Son Ltd., London, 1967).

¹⁷R. A. Waldron, *Theory of Guided Electromagnetic Waves* (Van Nostrand Reinhold Co., London, 1969).

¹⁸J. Halbritter, J. Appl. Phys. **41**, 4581 (1970).

¹⁹K. Simonyi, *Theoretische Elektrotechnik*, 9. durchgesehene Aufl. (VEB Deutscher Verlag der Wissenschaften, Berlin, 1989).

²⁰O. Klein, S. Donovan, M. Dressel, and G. Grüner, Int. J. Infrared Millim. Waves **14**, 2423 (1993).

²¹K. S. Champlin and R. R. Krongard, IRE Trans. Microwave Theory Tech. **MIT-9**, 545 (1961).

²²M. E. Brodwin and M. K. Parsons, J. Appl. Phys. **36**, 494 (1965).

²³L. I. Buravov and I. F. Shchegolev, Instrum. Exp. Tech. **14**, 528 (1971).

²⁴I. F. Shchegolev, Phys. Status Solidi A **12**, 9 (1972).

²⁵M. Cohen, S. K. Khanna, W. J. Gunning, A. F. Garito, and A. J. Heeger, Solid State Commun. **17**, 367 (1975).

²⁶H. W. Helberg and M. Dressel, J. Phys. I **6**, 1683 (1996).

²⁷N. P. Ong, J. Appl. Phys. **48**, 2935 (1977).

²⁸D.-N. Peligrad, B. Nebendahl, M. Mehring, A. Dulčić, M. Požek, and D. Paar, Phys. Rev. B **58**, 11 652 (1998).

²⁹J. Müller, Hochfrequenztechnik Elektroakustik **54**, 157 (1939).

³⁰C. J. F. Böttcher, *Theory of Electric Polarization*, 2nd ed. (Elsevier, Amsterdam, 1973), Vol. 1.

³¹J. D. Jackson, *Classical Electrodynamics*, 2nd ed. (Wiley, New York, 1987).

³²R. W. Morse and H. V. Bohm, Phys. Rev. **108**, 1094 (1957).

³³J. J. Bowman, T. B. A. Senior, and P. L. E. Uslenghi, *Electromagnetic and Acoustic Scattering by Simple Shapes* (Hemisphere, New York, 1987).

³⁴G. Schaumburg, H. W. Helberg, P. Berberich, and H. Kinder, Ann. Phys. (Leipzig) **1**, 584 (1992).

³⁵G. Schaumburg, Ph.D. thesis, Universität Göttingen, 1992.

³⁶G. Schaumburg and H. W. Helberg, J. Phys. III **4**, 917 (1994).

³⁷D.-N. Peligrad, Ph.D. thesis, Universität Stuttgart, 2001.

³⁸E. K. Hollmann, O. G. Vendik, A. G. Zaitsev, and B. T. Melekh, Supercond. Sci. Technol. **7**, 609 (1994).

³⁹B. Nebendahl, D.-N. Peligrad, M. Požek, A. Dulčić, and M. Mehring, Rev. Sci. Instrum. **72**, 1876 (2001).

⁴⁰B. Nebendahl, Ph.D. thesis, Universität Stuttgart, 2001.

⁴¹D. N. Peligrad, A. Dulčić, and M. Mehring (unpublished).